Journal of ELECTRONIC MATERIALS, Vol. 43, No. 1, 2014
DOI: 10.1007/s11664-013-2716-7

Structure–Property Correlations in CoFe–SiO_2 Nanogranular Films Utilizing x-Ray Photoelectron Spectroscopy and Small-Angle Scattering Techniques

P.R. OHODNICKI JR.,[1,2,7,8] V. SOKALSKI,[2] J. BALTRUS,[3] J.B. KORTRIGHT,[4] X. ZUO,[5] S. SHEN,[2] V. DEGEORGE,[2] M.E. MCHENRY,[2] and D.E. LAUGHLIN[2,6]

1.—Electrochemical and Magnetic Materials Team, Functional Materials Development Division, National Energy Technology Laboratory, United States Department of Energy, Pittsburgh, PA 15236, USA. 2.—Materials Science and Engineering Department, Carnegie Mellon University, Pittsburgh, PA 15213, USA. 3.—Chemistry and Surface Science Division, National Energy Technology Laboratory, United States Department of Energy, Pittsburgh, PA 15236, USA. 4.—Lawrence Berkeley National Laboratory, Berkeley, CA 94720, USA. 5.—X-ray Science Division, Argonne National Laboratory, Argonne, IL 60439, USA. 6.—Alcoa Professor of Physical Metallurgy, Carnegie Mellon University, Pittsburgh, PA 15213, USA. 7.—e-mail: paul.ohodnicki@gmail.com. 8.—e-mail: paul.ohodnicki@netl.doe.gov

A quantitative structure–property correlation study of thin films consisting of CoFe nanoparticles embedded in SiO_2 is presented, comparing film microstructure and chemistry with measured magnetic properties. SiO_2 was fully percolated for all films with $>\sim$50% SiO_2 by volume, and decreasing CoFe-nanoparticle size and separation with increasing SiO_2 resulted in a transition to superparamagnetic behavior. Partial oxidation of transition-metal elements is observed by x-ray photoelectron spectroscopy, and evidence for interparticle magnetic interactions can be resolved in soft x-ray resonant small-angle scattering experiments, highlighting the need for additional detailed and quantitative studies in this class of soft magnetic materials.

Key words: CoFe, nanogranular, superparamagnet, dipolar interactions, small-angle scattering, x-ray photoelectron spectroscopy

INTRODUCTION

Recent reports by the US Department of Energy indicate that 80% of all electricity is projected to flow through some form of power electronics by the year 2030.[1,2] Progressing power electronics with applications including improved converters for grid integration of advanced fossil fuel and renewable energy sources is therefore of increasing importance.[3,4] In addition, advanced inductor materials were recently identified as a high-priority area for enabling the next generation of power electronics devices capable of operating at higher frequencies and power densities.[2] A key consideration for development of advanced inductor materials for operation frequencies above $\sim$10 kHz is the increase in the loss contribution associated with classical and anomalous eddy currents, both of which scale inversely with the effective resistivity.[5] Ferrites have traditionally been employed for high-frequency inductor applications in the kHz to MHz range due to their large resistivities. However, ferrites are limited in high-power inductor applications due to their low saturation magnetization and poor thermal conductivity. A range of advanced soft magnetic nanocomposites composed of metallic nanoparticles with intergranular phases exhibiting high resistivity have therefore been developed.[6–17]

An example of extending the frequency response is provided by nanolaminated thin films,[18–20] where fast switching is achieved by limiting the thickness

(Received April 30, 2013; accepted July 29, 2013; published online August 29, 2013)

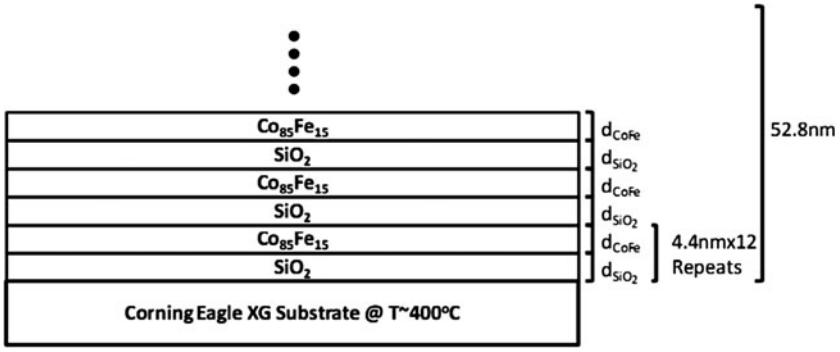

Fig. 1. Schematic of the multilayer deposition process used to synthesize $Co_{85}Fe_{15}$–SiO_2 nanogranular composite thin films. Note that the actual deposited film layers are not expected to be discrete and continuous due to the high deposition temperature and relatively thin layer thicknesses.

of the magnetic nanocomposite to stabilize Néel walls and alternating layers of a resistive oxide. Another example of this class of materials employs an insulating nonmagnetic oxide such as SiO_2 or Al_2O_3 to act as a percolating intergranular phase. These are synthesized by thin-film deposition techniques and are referred to as soft magnetic nanogranular films.[9,10,21] With a nonmagnetic intergranular phase, the magnetic properties of this class of materials are expected to be highly sensitive to the details of the film chemistry and the underlying microstructure, including the spatial composition distribution, particle size, interparticle spacing, and oxidation state of the elements. The strong structure sensitivity complicates attempts to scale up from thin-film geometries to the thick-film or bulk components required for relatively high-power applications while retaining technologically acceptable properties. Here we discuss an investigation of film microstructure, chemistry, and measured properties in model systems consisting of CoFe–SiO_2 thin films fabricated by sputter-deposition techniques, which may elucidate information relevant to bulk and thin-film systems. We focus on DC magnetic properties here, but future investigations taking similar approaches may also provide insights into the high-frequency responses of this class of materials.

EXPERIMENTAL PROCEDURES

CoFe–SiO_2 composite thin films were deposited using a high-temperature, multilayer deposition process to ensure uniformity of the underlying film microstructure and tunability of the relative volume fraction of CoFe and SiO_2 for fixed overall film thickness. A schematic of the deposition process is illustrated in Fig. 1, showing that film layers of ~4.4 nm total thickness and consisting of sublayers of $Co_{85}Fe_{15}$ and SiO_2 were repeated 12 times for a total film thickness of ~52.8 nm. All layers were deposited by radio frequency (RF) sputtering after achieving a base pressure of $< 5 \times 10^{-7}$ torr in a flowing Ar atmosphere of 5 mtorr on a Corning Eagle XG glass substrate at temperature of ~400°C. Using this approach, the total volume fraction of SiO_2 in the film could be tuned by varying the relative thicknesses of the SiO_2 and $Co_{85}Fe_{15}$ layers. The $Co_{85}Fe_{15}$ composition was selected due to the relatively low magnetostriction that is typically observed for high-Co-containing CoFe-based alloys, which can play an important role in measured magnetization responses.[5]

Synthesized films were characterized by transmission electron microscopy (TEM), x-ray photoelectron spectroscopy (XPS), x-ray diffraction (XRD) analysis, and alternating gradient magnetometry (AGM). Plan-view TEM was performed on films that were deposited directly on Si_3N_4 membrane grids for ease of sample preparation using a JEOL 2000EX microscope operating at 200 kV. Cross-sectional TEM samples were prepared from films deposited on glass substrates using standard focused ion beam lift-out techniques and subsequently mounted on Cu grids for imaging using a Tecnai F20 microscope at 200 kV. Particle size estimates, referred to as D_{TEM} below, were obtained from plan-view TEM images by image processing. Due to overlap between the particles throughout the film thickness, manual tracings of particles were performed for several TEM images obtained from different locations of the film. The tracings were subsequently thresholded and analyzed using standard image processing tools available in ImageJ; in particular, the "Analyze Particles" macro was employed to estimate the mean and standard deviation of estimated particle diameter.

XRD was performed using an Elvis Xpert diffractometer in standard Bragg–Brentano geometry such that only crystallographic planes parallel to the film surface gave rise to measurable diffraction intensity. XPS measurements were performed with a PHI 5600ci spectrometer using a Mg K_α x-ray source and an analyzer pass energy of 58.7 eV. Binding energies were referenced to the Si 2s peak at 153.8 eV. Compositions were calculated from peak areas using sensitivity factors provided by the instrument manufacturer. Simple curve fitting of the Co $2p_{3/2}$ and Fe $2p_{3/2}$ spectra to obtain the relative fractions of oxidized Co and Fe was accomplished using CasaXPS software; the minimum number of peaks required to obtain a satisfactory overall fit were used. Elemental depth profiles were

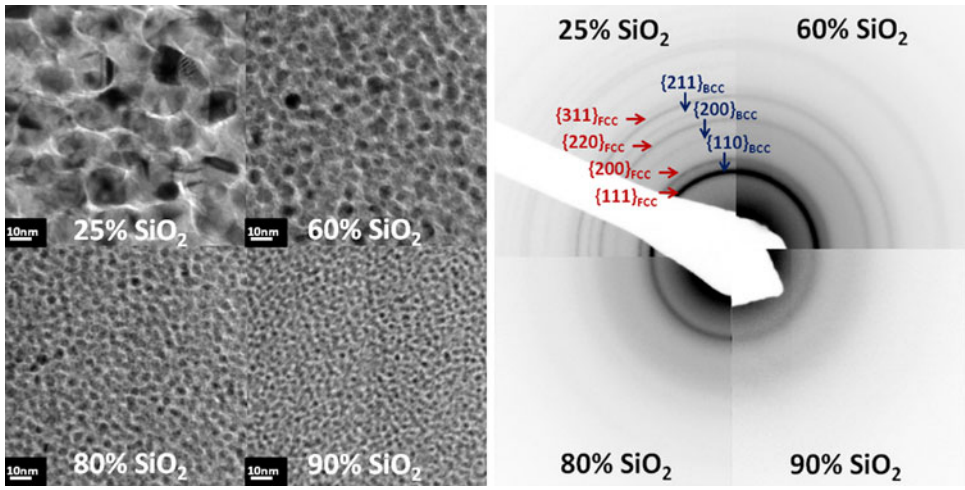

Fig. 2. Plan-view transmission electron microscopy images and corresponding SAD patterns of $Co_{85}Fe_{15}$–SiO_2 thin films with varying SiO_2 content by volume. Refinement of the CoFe grain size, formation of an intergranular SiO_2 phase, and broadening of the SAD pattern rings are observed with increasing SiO_2 content. BCC phase rings become relatively weak as compared with FCC with increasing SiO_2 content, and only the lowest-order rings are clearly resolved for the highest SiO_2 content films.

measured by alternation of XPS analysis with sputtering of the surface by an Ar^+ ion beam. A differentially pumped ion gun was operated at 1.5×10^{-2} Pa and 25 mA to deliver a sputtering rate of ~8.5 nm/min.

Small-angle scattering experiments were also performed on selected thin-film samples to quantify the characteristic length scales of the microstructure under investigation. Scattering experiments were performed on beamline 12ID-B at Argonne National Laboratory for thin-film samples on glass substrates to probe scattering due solely to charge/chemical heterogeneities of the sample under investigation. In all cases, a corresponding measurement was performed for a blank glass substrate and subtracted from measurements performed on the film samples. Soft x-ray resonant scattering was performed on beamlines 11.0.1 and 6.3.2 at Lawrence Berkeley National Laboratory's Advanced Light Source to allow for additional contributions to measured scattering intensity associated with heterogeneities in the magnetization distribution within the sample. By tuning near the Co L_3 absorption edge at 778 eV, the resonant magnetic term in the scattering factor is dramatically enhanced, allowing angle-resolved measurements of magnetic correlation lengths in addition to chemical correlation lengths. Samples consisted of single multilayer films deposited on a silicon nitride membrane mounted with surface normal along the incoming, linearly polarized x-ray beam. Scattering was measured by scanning an apertured detector through a low angle range with the scattering vector in the film plane.[22,23]

RESULTS AND DISCUSSION

CoFe–SiO_2 films were deposited with nominal SiO_2 volume fraction ranging between 0% and 90%. Plan-view TEM images obtained for selected samples are presented in Fig. 2, illustrating a clear refinement in the particle size of CoFe grains and the formation of an intergranular SiO_2 layer with increasing SiO_2 content. For the films with SiO_2 volume fractions of 50% and greater, the intergranular SiO_2 phase appears to be percolated based upon acquired TEM images, which is consistent with expectations from prior reports where the percolation limit typically occurs at volume fractions between 40% and 60%.[24] Further evidence for film percolation was obtained by four-point probe measurements of sheet resistance using a setup commonly employed for metallic thin films, for which no measurable value could be resolved for samples with SiO_2 content ≥50%, suggesting a percolated, electrically insulating microstructure. Selected-area diffraction (SAD) patterns for these films are also presented, confirming a two-phase mixture of body-centered cubic (BCC) and face-centered cubic (FCC) CoFe grains for the 25% SiO_2 sample, as would be expected given that the Co:Fe ratio places the alloy in the two-phase BCC + FCC region of the CoFe phase diagram at the deposition temperature.[17,25] With increasing SiO_2 content, all of the observed rings also broaden, which is consistent with decreasing particle size. A decrease in the relative intensity of the rings indexed to BCC as compared with FCC was also observed with increasing SiO_2 content, suggesting that the relative amount of FCC may be increasing. In the case of the 80% and 90% SiO_2 films, only a single, broad ring could be clearly resolved, at a d-spacing corresponding approximately to the lowest index ring of FCC or BCC. Figure 3 presents cross-sectional TEM images for three films with >50% SiO_2 content, illustrating that the films consist of spherical CoFe nanoparticles separated by an intergranular SiO_2 phase.

x-Ray photoelectron spectroscopy experiments performed on deposited films can provide information about the spatial variation of composition

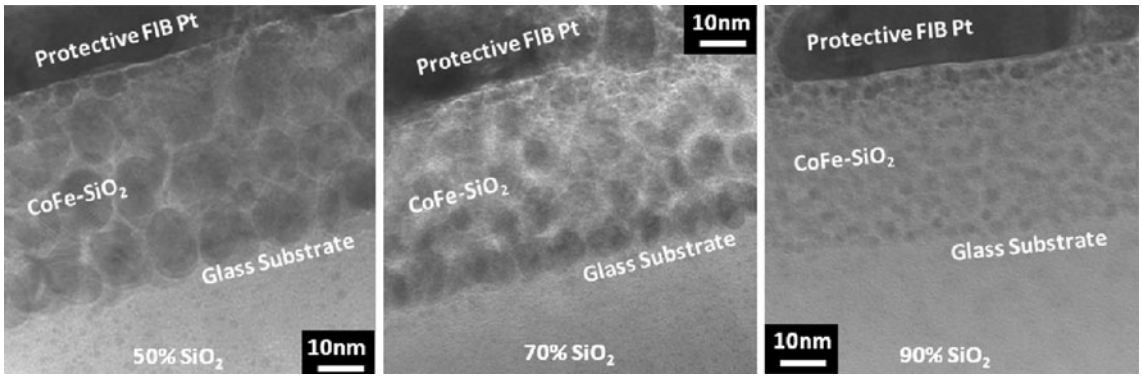

Fig. 3. Cross-sectional TEM images of CoFe–SiO_2 films with 50%, 70%, and 90% SiO_2 content, illustrating that the microstructure consists of spherical particles embedded in an intergranular phase of SiO_2 over this film composition range. The film is coated with a layer of protective Pt during the focused ion beam (FIB) lift-out process.

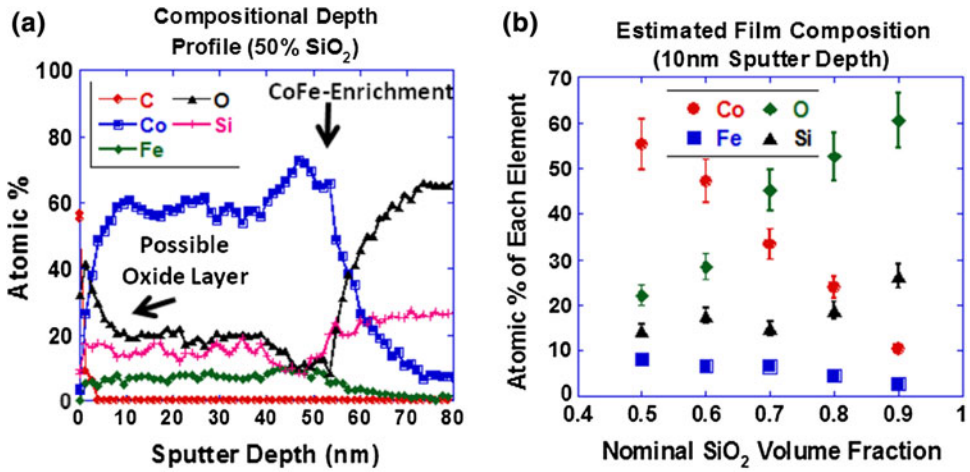

Fig. 4. (a) Sputter depth composition profile obtained using XPS for a 50% SiO_2 film, illustrating enrichment of Co and Fe near the glass substrate and a possible oxidation layer at the top surface of ~7 nm in thickness. (b) Estimated film composition as a function of SiO_2 content based on XPS spectra measured at ~10 nm into the film depth. A discontinuity can be observed for the samples with 70% and greater SiO_2, consistent with an increase in the relative degree of transition-metal element oxidation in these films.

through the depth of the film as well as the oxidation state of all elements in the composite microstructure. An example of a measured compositional depth profile obtained from the 50% SiO_2 sample is presented in Fig. 4a. For this sample there is potential evidence for enrichment in Co and Fe near the substrate, suggesting a higher density of CoFe nanoparticles during initial film growth. A gradual decrease in oxygen and an increase in Co over a depth of ~7 nm were also observed near the film surface, corresponding to enhanced oxidation at the surface. To estimate the film composition as a function of SiO_2 content, the top ~10 nm of each film was sputtered away to remove surface contamination and high-resolution spectra of Co, Fe, Si, and O were measured. The results for films with SiO_2 contents ranging between 50% and 90% are presented in Fig. 4b, illustrating a monotonic decrease in Co and Fe with increasing SiO_2 content and an overall increase in both Si and O, as would be expected.

Comparing the measured XPS Fe 2p and Co 2p spectra in Fig. 5 for the deposited films containing 60% and 90% SiO_2, Fe is observed to be more heavily oxidized than Co and the degree of oxidation is larger for the highest SiO_2 content films. Preferential oxidation of Fe could explain the decrease in relative intensity of BCC as compared with FCC diffraction rings in measured SAD patterns with increasing SiO_2 content of the film (Fig. 2). A slight discontinuity in the measured O and Si composition of the films with SiO_2 volume fractions >60% is observed in Fig. 4b, which correlates with a noticeable increase in the degree to which Fe and Co are oxidized based upon measured Fe 2p and Co 2p spectra; For example, the curve-fitting results of the measured Fe 2p and Co 2p peaks in Fig. 5c, d illustrate that Fe is almost fully oxidized and that Co is heavily oxidized for the 90% SiO_2 sample. A table of results of standard peak-fitting procedures of the type illustrated in Fig. 5a–d is also presented. The lack of clearly resolved higher-order diffraction

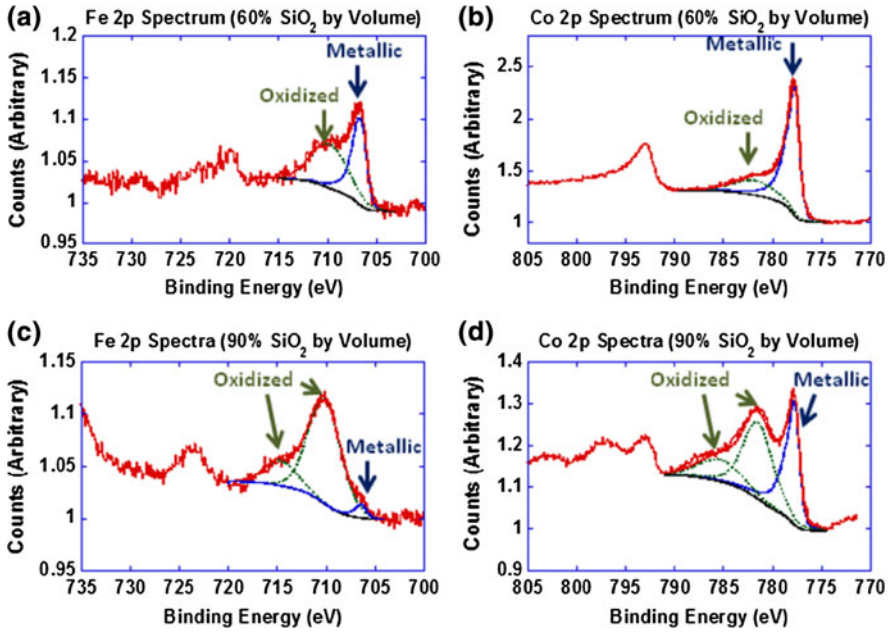

% SiO_2	% Co oxidized	% Fe Oxidized
50	24.1	43.9
60	33.0	52.2
70	64.4	91.1
80	70.8	95.0
90	72.3	95.8

Fig. 5. Fe and Co 2p spectra measured after sputtering away the top 10 nm of the 60% and 90% SiO_2 films. As illustrated by the peak-fitting results for the Fe and Co $2p_{3/2}$ peaks, intensity is observed at binding energies corresponding to higher oxidation states of Fe and Co (indicated by "oxidized," dashed green) in addition to expected intensity at binding energies corresponding to "metallic" Fe and Co (solid blue). The assumed background (solid black) and fitted envelope (solid red) are also presented. A larger relative degree of Fe oxidation as compared with Co for all films as well as a greater degree of relative transition-metal oxidation for the highest SiO_2 content films can be observed, as summarized in the table based upon integration of fits of the type illustrated (Color figure online).

rings for the highest SiO_2 content films could also be linked with a relatively large degree of Fe and Co oxidation. Subsequently, films deposited under similar processing conditions have shown variation in the degree of Fe and Co oxidation, suggesting that further work is required to understand the process parameters that can affect the degree of oxidation of the transition-metal elements. Although care was taken to ensure that samples were not exposed to ambient atmosphere at temperatures $>100°C$, we cannot completely rule out some degree of postdeposition film oxidation that may occur upon cooling following the high-temperature deposition. Follow-up experiments are currently underway for samples in which a SiO_2 capping layer is employed prior to exposing the films to ambient atmosphere to further minimize the potential for postdeposition oxidation.

DC magnetic properties of the synthesized films were measured, and representative hysteresis loops for the 50%, 60%, and 80% SiO_2 samples as measured at room temperature are presented in Fig. 6 along with plots of the saturation magnetization and coercivity as a function of SiO_2 content. Above 50% SiO_2 content, the microstructure can be described as CoFe particles embedded in a continuous SiO_2 matrix. A characteristic shearing of the hysteresis loop occurs with increasing SiO_2, resulting in decreased susceptibility, coercivity, and remanence. Accordingly, the squareness (defined as the ratio of the remanent to saturation magnetization) decreases from a value of $\sim$0.7 for the 50% SiO_2 film to a value of $\sim$0.01 for the 80% SiO_2 film. The observed trends are consistent with a transition towards superparamagnetic behavior with increasing SiO_2 content and decreasing CoFe particle size. For the 90% SiO_2 film, the low absolute signal prevented us from estimating a coercivity value with confidence. The expected trend of decreasing M_s with increasing SiO_2 volume fraction is observed, although the measured values of M_s appear somewhat lower than the value expected based upon the nominal SiO_2 volume fraction using the moment of pure Co for the magnetic phase. The experimentally observed partial oxidation of the transition-metal elements in the films could be one explanation.

It is well known that small-angle x-ray scattering (SAXS) experiments can be employed for quantitative studies of microstructural features in the case of characteristic length scales ranging from $\sim$1 nm to 100 nm.[26] The scattered intensity for a single scattering site is described by Eq. 1.[27,28]

$$I(Q) = NV_S^2|\Delta\rho|^2P(Q)S(Q) + I_{\text{background}}. \quad (1)$$

In Eq. 1, Q is the scattering vector, P is the form factor, N is the number of particles per unit volume, V_S is the volume of the particle, and $\Delta\rho$ is the contrast scattering length or the extra electron density of the particle over the dispersion matrix. $S(Q)$ corresponds to the structure factor, which describes interference between closely spaced scattering sites and can provide information about interparticle

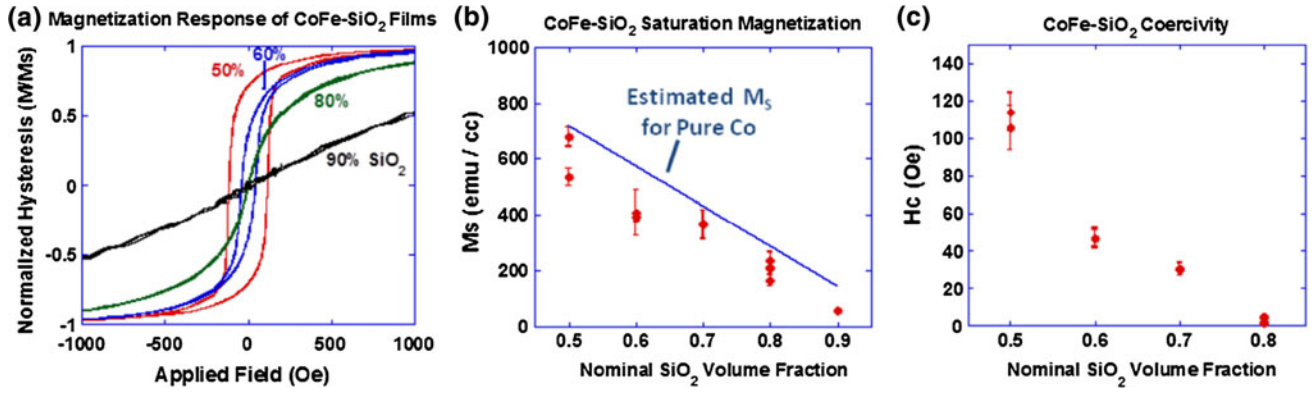

Fig. 6. (a) Representative hysteresis loops measured for samples with varying SiO_2 content and normalized relative to the measured value of M_s. (b) Measured trend in M_s as a function of SiO_2 content in synthesized films along with the estimated value for the corresponding volume fraction of FCC Co for comparison (solid line). (c) Measured coercivity of synthesized films as a function of SiO_2 content.

spacing and packing. The distance between nearest particles can be approximated as $2\pi/Q_{peak}$, where Q_{peak} is the position of the first intensity maximum.[22] SAXS measurements performed at energies corresponding to hard x-rays, which are expected to be sensitive only to film microstructure, are presented in Fig. 7a, illustrating a clear peak in scattering that decreases in intensity and shifts to increasing Q with increasing SiO_2 content of the film. It has been shown that aggregates of closely spaced particles or precipitates can result in a peak in small-angle scattering intensity that is closely related to interparticle spacing, which explains the observed peak in scattering reported here.[22] The observed trends are consistent with a decreasing size and volume fraction and an increased interparticle spacing of the CoFe-based nanoparticle phase. No significant SAXS contrast could be observed for the 90% SiO_2 films above the background level, and hence these results are not included. The weak scattering contrast for this sample may be due to the low volume fraction of the CoFe-based nanoparticles and almost complete oxidation of the transition-metal elements. Figure 7b illustrates the estimated interparticle spacing as a function of SiO_2 content calculated from the peak in small-angle scattering data (D_{SAXS}) along with esti mated grain sizes of CoFe nanoparticles from plan-view images (D_{TEM}) such as those presented in Fig. 2a.

Using the values of D_{SAXS} and D_{TEM} presented in Fig. 7b, the experimentally measured coercivities (H_C) of Fig. 6c were fit to the assumed power-law dependence of Eq. 2 over the film composition range of ~50% to 80% SiO_2.

$$H_C = H_C^0 D^X. \tag{2}$$

In Eq. 2, H_C^0 is a fitted constant prefactor, X is a fitted exponent, and D is the experimental value of particle size (D_{TEM}) or interparticle spacing (D_{SAXS}). The form of Eq. 2 was chosen based upon well-known empirical relationships between coercivity and average grain size in exchange-coupled soft magnetic materials. These systems tend to follow a power-law dependence with X values of ~ -1 associated with domain-wall pinning at grain boundaries for large-grained materials and ranging between ~3 and 6 for nanocrystalline or nanocomposite systems due to effective averaging of the magnetocrystalline anisotropy over many grains.[5,29] For assemblies of exchange-decoupled magnetic particles, larger particles with sizes above the critical single-domain limit also have been shown to exhibit power-law dependences with $X \approx -1$, while smaller particles with sizes approaching the superparamagnetic limit instead have been shown to exhibit a different particle size dependence of the form $H_C = K(1 + (D_P/D)^{3/2})$, where D_P here is the assumed upper particle diameter for superparamagnetic behavior and K is a function of the magnetocrystalline anisotropy and saturation magneti zation of the particles.[30] The authors also theoretically justified the latter expression in the case of particles with uniaxial magnetic anisotropy. As a result, the data presented here were also fit to a second assumed power-law dependence with an additional offset term:

$$H_C = H_C^1 + H_C^0 D^X, \tag{3}$$

The terms in Eq. 3 retain the same meanings as those presented in Eq. 2 with H_C^1 corresponding to an additional fitted constant.

The results of the fitting procedure are presented in Fig. 7c, d, in which solid lines correspond to fits to Eq. 2 and dashed lines correspond to fits to Eq. 3. Both D_{SAXS} and D_{TEM} were utilized for the fitting of experimental coercivity data because of a lack of detailed understanding of the magnetization process of systems with weak or negligible exchange coupling between particles. For isolated particles, D_{TEM} is expected to be the primary parameter dictating the measured coercivity, but for particle assemblies that exhibit significant dipolar interactions,

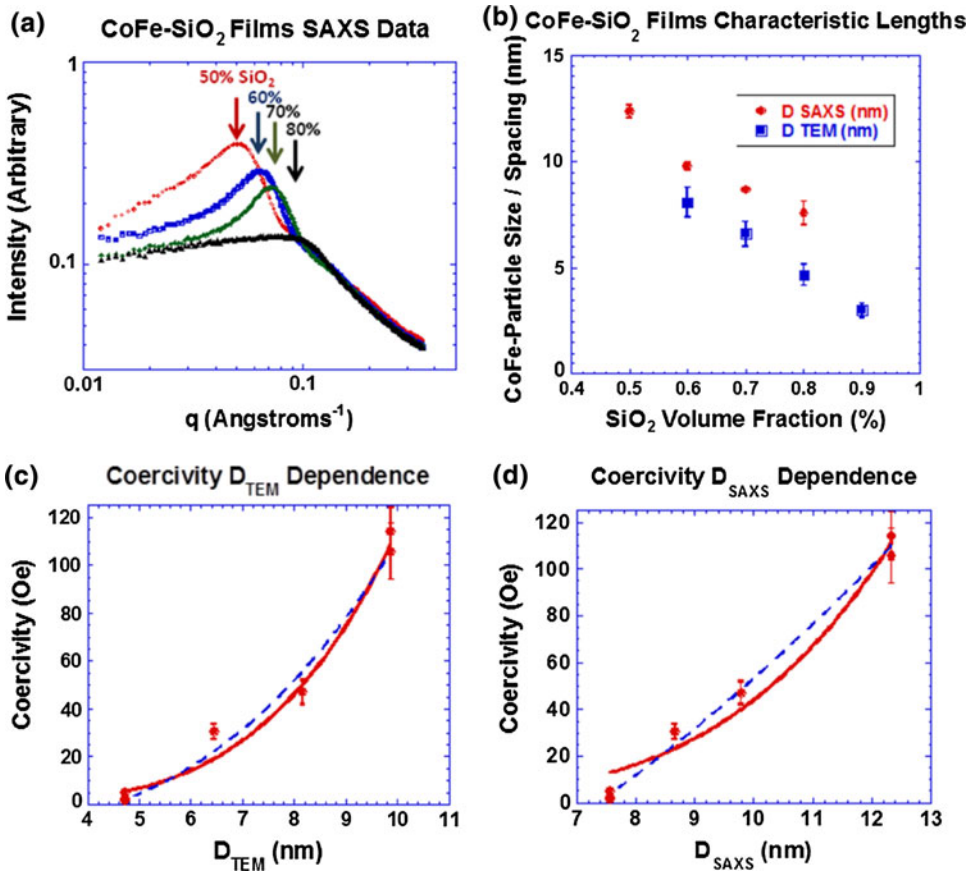

Fig. 7. (a) Small-angle scattering data for selected CoFe–SiO_2 films with nominal SiO_2 volume fractions of 50% to 80% as labeled. (b) Estimated interparticle spacing from small-angle scattering data (D_{SAXS}) and estimated CoFe particle size from plan-view TEM images (D_{TEM}). (c) and (d) illustrate the estimated trends in coercivity as a function of D_{SAXS} and D_{TEM} fit to a power-law expression over the same film composition range as (a). Solid and dashed lines correspond to fits using Eqs 2 and 3, respectively.

D_{SAXS} may instead prove to be the dominant parameter, as such interactions have been proposed as a source of coercivity in assemblies of interacting superparamagnetic particles.[31,32] Estimated values of X from the fitting process range from ~3.5 to 5 when fitting uncertainty is considered in the case where Eq. 2 is used ($X \approx 4 \pm 0.5$ for D_{TEM}, $X \approx 4.4 \pm 0.6$ for D_{SAXS}). In the case of fits using Eq. 3, greater sensitivity of the fitting results to the assumed initial values of the parameters and relatively large uncertainties were observed due to the limited number of data points and the additional fitting parameter. Smaller values of X appear to provide the best fitting results in this case with $X \approx 3 \pm 0.75$ for D_{TEM} and $X \approx 1.7 \pm 0.6$ for D_{SAXS}. However, the fits also result in negative fitted values of H_C^1, which cannot be justified based upon the physical origin of this constant for the model of noninteracting superparamagnetic particle assemblies motivating the use of the expression.[30] The reduced value of X and the negative estimated values of H_C^1 are particularly evident for the fit to D_{SAXS}, where $H_C^1 \approx -75 \pm 35$ Oe was estimated.

It has been shown that SAXS experiments performed using lower-energy (i.e., soft) x-rays can simultaneously provide information about characteristic length scales of heterogeneity in both the charge/chemical structure and the corresponding magnetic structure.[22,33] The origin of the additional contrast associated with the magnetic structure is due to the resonant magnetic contributions to the scattering factor that become comparable to the charge contribution at the Co L_3 edge in the soft x-ray range.[22,23] Soft x-ray SAXS results for samples prepared in a similar manner to those described above are presented in Fig. 8, illustrating scattering peaks associated with the charge/chemical heterogeneity for all films which are consistent with measurements performed using hard x-rays (Fig. 8b). For the films with 60% and 80% SiO_2 content, additional contrast associated with the magnetic scattering contribution is observed at lower Q values, indicating that the underlying spin structure exhibits a periodicity approximately a factor of 2 to 3 times greater than that of the interparticle spacing (Fig. 8b). Larger characteristic length scales associated with heterogeneity in the magnetic structure as compared with the interparticle spacing can often be attributed to magnetic interactions between particles with dipolar interactions

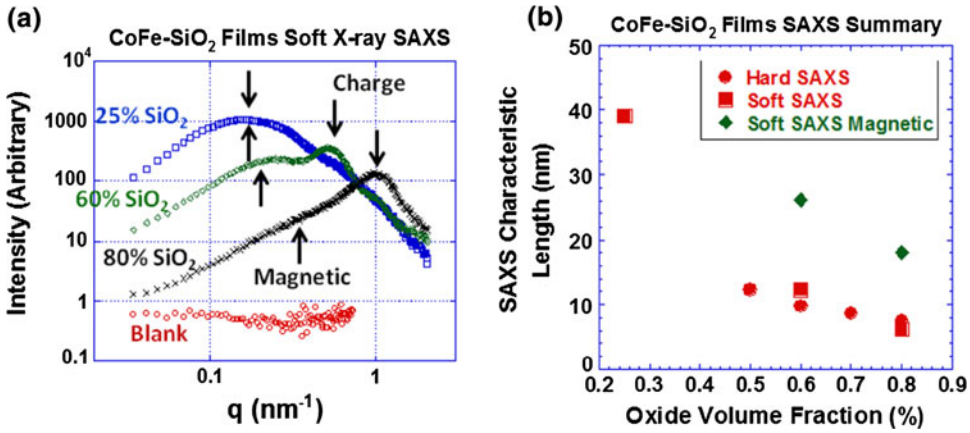

Fig. 8. (a) Soft x-ray small-angle scattering data for CoFe–SiO_2 films with nominal SiO_2 volume fractions of 25%, 60%, and 80% as labeled. Downward-oriented arrows indicate peaks due to charge/chemical heterogeneity, while upward-oriented arrows indicate contrast features arising from magnetic heterogeneity. (b) Estimated interparticle spacing from both hard and soft x-ray SAXS data as well as the estimated characteristic length associated with the magnetic contribution to the scattering.

whose moments vary widely in orientation relative to each other.[22,33,34] Strict nearest-neighbor antiferromagnetic (AF) moment orientations would yield a magnetic peak at half of the Q value of the chemical peak, while a broader dispersion of moment orientations would manifest as a broader magnetic intensity distribution in the scattered intensity.[25] In the case of the 25% SiO_2 film, a single, broad scattering peak is resolved, which is consistent with the onset of a percolated CoFe phase resulting in intergranular exchange coupling, and ferromagnetically aligned spins.[22] In this case, magnetic and chemical heterogeneity both contribute at the same length scale, as ferromagnetically aligned CoFe has magnetic heterogeneity defined simply by the chemical heterogeneity.

Prior investigations of samples consisting of CoFe-based nanoparticle assemblies embedded in a nonmagnetic matrix have provided evidence for magnetic interactions between the particles impacting the measured DC hysteresis response as well as correlations between spin orientations in adjacent nanoparticles. Prior works on Co-nanoparticle assemblies,[22] Co–SiO_2 composite films,[34] and Fe-based metallic/amorphous nanocomposites well above the Curie temperature of the amorphous phase[31] have concluded that dipolar interactions are the primary mechanism responsible for intergranular magnetic interactions. For the Fe-based nanocomposites it has been demonstrated that such interactions can result in a source of measured coercivity as compared with noninteracting superparamagnetic particles of the same size.[31] In the case of Co-nanoparticle assemblies and Co–SiO_2 composite films, spatial correlations in the orientations of moments in adjacent particles due to dipolar interactions have been reported based upon soft x-ray or neutron small-angle scattering experiments.[33,34] Because long-range dipolar interactions are expected to depend upon both the relative orientations of the magnetic moments as well as the interparticle spacings,[33–37] the degree of interaction is expected to depend strongly upon both the interparticle separation and the way in which particles are packed to form the composite film. Other operative mechanisms for magnetic coupling in thin films and multilayers include orange-peel[38–40] and pinhole coupling. Adherent oxides on FeCo make pinhole coupling unlikely, but the large magnetization of FeCo amplifies the importance of magnetostatic interactions responsible for orange-peel coupling. Possibilities of intergranular exchange interactions between particles in direct contact also arise in the case where clusters of particles rather than isolated particles are surrounded by the intergranular insulating oxide phase, as reported by previous authors.[41] Such details are expected to play an important role in DC as well as high-frequency magnetization processes, and the temperature dependence of the DC magnetization of such materials can sometimes help to distinguish between different coupling mechanisms.[20] The quantitative fits to the measured coercivity data presented here in Fig. 7 should be interpreted with caution due to the observed partial oxidation of transition-metal elements in the synthesized films and the limited number of data points. Additional studies of the type described here coupled with appropriate theoretical models can be expected to yield important insights useful for understanding and optimizing this relatively new class of soft magnetic materials.

CONCLUSIONS

A systematic investigation of $Co_{85}Fe_{15}$–SiO_2 thin films of fixed thickness was performed as a function of the nominal volume fraction of SiO_2. Decreasing CoFe-nanoparticle size and spacing with increasing SiO_2 volume fraction was observed over the range of SiO_2 contents investigated. Films containing $\geq\sim$50% SiO_2 by volume exhibited a percolated oxide phase

and a composite microstructure of CoFe-based nanoparticles surrounded by a SiO_2 intergranular phase. The degree of oxidation of the transition-metal elements was investigated by XPS, showing that Fe was preferentially oxidized relative to Co during the deposition process and that the degree of oxidation was largest in the films prepared with the highest SiO_2 volume fraction. Measured trends in magnetic properties are discussed as a function of SiO_2 content, CoFe particle size, and interparticle separation. Small-angle scattering experiments performed with soft x-rays elucidated characteristic length scales of the magnetic structure to be ~2 to 3 times the interparticle spacing and suggest potential evidence for interparticle magnetic interactions. Additional quantitative studies are needed to clarify the magnetization processes (both DC and high frequency) in this class of materials, as details such as particle size, interparticle separation, and the partial oxidation of transition-metal elements would be expected to have a strong impact on the magnitude and type of interparticle magnetic coupling.

ACKNOWLEDGEMENTS

Use of the Advanced Photon Source, an Office of Science User Facility operated for the US Department of Energy (DOE) Office of Science by Argonne National Laboratory, was supported by the US DOE under Contract No. DE-AC02-06CH11357. M.E.M. and D.E.L. acknowledge support of the NSF through Grant No. DMR #0804020.

REFERENCES

1. R. Ram, R.R. *Power Electronics in Photovoltaic Systems*. 2011. http://arpa-e.energy.gov/EventsWorkshops/PastWorkshops/PowerElectronicsinPhotovoltaicSystems.aspx. Accessed Dec 2012.
2. Ram, R. *Power Electronics*. 2010. http://arpa-e.energy.gov/Portals/0/Documents/ConferencesAndEvents/PastWorkshops/2010InnovationSummit/PowerElectronics_Ram.pdf. Accessed Dec 2012.
3. Hefner, A., *High Megawatt Converter Workshop*, Gaithersburg, MD, 2007.
4. Hefner, A. *High-Voltage, High-Frequency Devices for Solid State Power Substation and Grid Power Converters*. In *High Megawatt Power Converter Technology R&D Roadmap Workshop* 2008. Gaithersburg, MD.
5. R.C. O'Handley, *Modern Magnetic Materials: Principles and Applications* (New York: Wiley, 2000).
6. Y.S.O. Yoshizawa and K. Yamauchi, *J. Appl. Phys.* 64, 6044–6046 (1988).
7. K. Suzuki, A.M.A. Inoue, and T. Masumoto, *J. Appl. Phys.* 70, 6232–6237 (1991).
8. M. McHenry and D.E. Laughlin, *Prog. Mater. Sci.* 44, 291–433 (1999).
9. S. Ohnuma, M. Ohnuma, H. Fujimori, and T. Masumoto, *J. Magn. Magn. Mater.* 310, 2503–2509 (2007).
10. W. Li, Y. Sun, and C.R. Sullivan, *IEEE Trans. Magn.* 41, 3283–3285 (2005).
11. A. Leary, P.R. Ohodnicki, and M. McHenry, *J. Met.* 64, 722–781 (2012).
12. S. Shen, P.R. Ohodnicki, S. Kernion, A. Leary, V. Keylin, J. Huth, and M. E. McHenry. *Nanocomposite alloy design for high frequency power conversion applications*. In *TMS Annual 2012*. 2012. Orlando, FL.
13. P.R. Ohodnicki, J. L, D.E. Laughlin, M.E. McHenry, V. Keylin, and J. Huth, *J. Appl. Phys.* 104, 113909–113915 (2008).
14. P.R. Ohodnicki, S.Y. Park, D.E. Laughlin, M.E. McHenry, V. Keylin, and M.A. Willard, *J. Appl. Phys.* 103, 07E729–07E731 (2008).
15. M.A. Willard, D.E. L, and M.E. McHenry, *J. Appl. Phys.* 87, 7091–7096 (2000).
16. M.A. Willard, M.Q. H, D.E. Laughlin, M.E. McHenry, J.O. Cross, and V.G. Harris, *J. Appl. Phys.* 85, 4421–4423 (1999).
17. P.R. Ohodnicki, Y. L.Q, D.E. Laughlin, M.E. McHenry, M. Kodzuka, T. Ohkubo, K. Hono, and M.A. Willard, *Acta Mater.* 57, 87–96 (2009).
18. H. Okumura, C.Y. U, M.E. McHenry, S. Chu, D.E. Laughlin, and A.B. Kos, *IEEE Trans. Magn.* 40, 2700–2702 (2004).
19. H. Okumura, D.J. T, R.D. McMichael, M.Q. Huang, Y.N. Hsu, M.E. McHenry, and D.E. Laughlin, *J. Appl. Phys.* 95, 6528–6530 (2003).
20. M.Q. Huang, Y.N. H, M.E. McHenry, and D.E. Laughlin, *IEEE Trans. Magn.* 37, 2239–2241 (2001).
21. R.S. Ishkhakov, G.I. F, V.S. Zhigalov, and D.E. Prokof'ev, *Tech. Phys. Lett.* 30, 687–689 (2004).
22. E. Fullerton, O. H, Y. Ikeda, B. Lengsfield, K. Takano, and J. Kortright, *IEEE Trans. Magn.* 38, 1693–1696 (2002).
23. J.B. Kortright, K. Sang-Koog, G.P. Denbeaux, G. Zeltzer, K. Takano, and E.E. Fullerton, *Phys. Rev. B* 64, 092401 (2001).
24. P. Sheng, *Electronic Transport in Granular Metal Films, Nanophase Materials* (Dordrecht: Kluwer Academic, 1994).
25. P. Ohodnicki, et al., *Acta Mater.* 58, 4804–4813 (2010).
26. F.D. Geuser and A. D, *C. R. Phys.* 13, 246–256 (2012).
27. R. Borsali, R. Pecora, eds., *Soft-Matter Characterization*. (Berlin: Springer, 2008).
28. E. Huang, P.K. Liaw, L. Porcar, Y. Liu, Y. Liu, J. Kai, and W. Chen, *Appl. Phys. Lett.* 93, 161904-1–161904-4 (2008).
29. K. Suzuki and J.M. Cadogan, *Phys. Rev. B* 58, 2730–2739 (1998).
30. E.F. Kneller and F.E. L, *J. Appl. Phys.* 34, 656–658 (1963).
31. V. Franco, C.F. Conde, and A. Conde, *Phys. Rev. B* 72, 174424-1–174424-10 (2005).
32. P. Allia, M. Coisson, M. Knobel, P. Tiberto, and F. Vinai, *Phys. Rev. B* 60, 12207–12218 (1999).
33. J.B. Kortright, O. Helllwig, K. Chesnel, S. Sun, and E.E. Fullerton, *Phys. Rev. B* 71, 012402-1–012402-4 (2005).
34. S. Sankar, D. Dender, J.A. Borchers, D.J. Smith, R.W. Erwin, S.R. Kline, and A.E. Berkowitz, *J. Magn. Magn. Mater.* 221, 1–9 (2000).
35. S. Bedanta, T. Eimüller, W. Kleeman, J. Rhensius, F. Stromberg, E. Amaladass, S. Cardoso, and P.P. Freitas, *Phys. Rev. Lett.* 98, 176601-1–176601-4 (2007).
36. M. Knobel, W.C. N, A.L. Brandl, J.M. Vargas, L.M. Socolovsky, and D. Zanchet, *Phys. B* 354, 80–87 (2004).
37. S. Morup, M.F. Hansen, and C. Frandsen, *Beilstein J. Nanotechnol.* 1, 182–190 (2010).
38. L. Neel, *Comptes Rendus* 255, 1676 (1962).
39. B. Dieny, V.S. S, S.S. Parkin, B.A. Gurney, D.R. Wilhoit, and D. Mauri, *Phys. Rev.* B43, 1297 (1991).
40. J. Zhang and R.M. W, *IEEE Trans. Magn.* 32, 4630 (1996).
41. Y. Yang, L. Z, W. Lan, and X. Bi, *Rare Met.* 30, 533–537 (2011).